Growth and collapse of cavitation bubbles near a curved rigid boundary

By Y. TOMITA[1], P. B. ROBINSON[2], R. P. TONG[3]
AND J. R. BLAKE[2]

[1]Faculty of Education, Hokkaido University of Education, Hakodate, 1-2 Hachiman-cho, Hakodate, Hokkaido, Japan

[2]School of Mathematics and Statistics, University of Birmingham, Edgbaston, Birmingham B15 2TT, UK

[3]The Numerical Algorithms Group Ltd, Jordan Hill Road, Oxford OX2 8DR, UK

Laser-induced cavitation bubbles near a curved rigid boundary are observed experimentally using high-speed photography. An image theory is applied to obtain information on global bubble motion while a boundary integral method is employed to gain a more detailed understanding of the behaviour of a liquid jet that threads a collapsing bubble, creating a toroidal bubble. Comparisons between the theory and experiment show that when a comparable sized bubble is located near a rigid boundary the bubble motion is significantly influenced by the surface curvature of the boundary, which is characterized by a parameter ξ, giving convex walls for $\xi < 1$, concave walls for $\xi > 1$ and a flat wall when $\xi = 1$. If a boundary is slightly concave, the most pronounced migration occurs at the first bubble collapse. The velocity of a liquid jet impacting on the far side of the bubble surface tends to increase with decreasing parameter ξ. In the case of a convex boundary, the jet velocity is larger than that generated in the flat boundary case. Although the situation considered here is restricted to axisymmetric motion without mean flow, this result suggests that higher pressures can occur when cavitation bubbles collapse near a non-flat boundary. Bubble separation, including the pinch-off phenomenon, is observed in the final stage of the collapse of a bubble, with the oblate shape at its maximum volume attached to the surface of a convex boundary, followed by bubble splitting which is responsible for further bubble proliferation.

1. Introduction

As demonstrated by Benjamin & Ellis (1966), a solid boundary induces asymmetric flow around a bubble resulting in bubble migration toward the boundary due to the secondary Bjerknes force (Crum 1975; Pelekasis & Tsamopoulos 1993) and finally the formation of a liquid jet. It is now recognized that a major source of erosive forces is connected with the acoustic transient at the first and second collapses of the bubble very close to a boundary where a 'stand-off' parameter, $\gamma(= L/R_{max})$, defined as the ratio of initial bubble height above the boundary, L, to maximum bubble radius, R_{max}, is very important in understanding the bubble motion (Naudé & Ellis 1961; Blake, Taib & Doherty 1986; Tomita & Shima 1986; Vogel, Lauterborn & Timm 1989; Van der Meulen 1994).

Recently, the complicated physical process occurring during the very late stage of

the bubble collapse has been modelled by a numerical simulation by Best (1993) and Zhang, Duncan & Chahine (1993), and observed by ultra high-speed photography by Ohl, Philipp & Lauterborn (1995). The numerical calculations show the detailed flow structure after jet impact on the far side of the bubble surface, yielding a ring vortex flow of the toroidal bubble while the schlieren technique clearly captures a jet-impact-induced shock wave which occurs at a distance from the boundary surface before the bubble reaches a minimum volume. Philipp & Lauterborn (1998) carried out a very sophisticated experiment in order to elucidate the cause of cavitation erosion and reached the conclusion that the major cause of erosion is the pressure pulses produced by the collapse of a vortex ring bubble at its second collapse, which is basically the same idea as pointed out by Shutler & Mesler (1965). Philipp & Lauterborn (1998) found that the bubble shape is toroidal for $\gamma \leqq 1.7$ and the observed damage is in the shape of a circular ring as previously found by Shutler & Mesler (1965) and Tomita & Shima (1986), corresponding to the decay of the bubble torus into many tiny bubbles, each collapsing separately around the circumference of the torus. Since one of the key problems to be solved is concerned with the detailed characteristics of a liquid jet and the associated phenomena because a vortex ring bubble is formed as a result of the jet penetration through the bubble interior, Tong *et al.* (1999) and Blake, Tomita & Tong (1998) undertook an investigation of the dynamics of a liquid microjet during the bubble collapse, particularly by taking account of the role of 'splashing' generated after a toroidal bubble is created.

As is well known, pressure amplification occurs due to the interaction between a shock wave and a bubble (Tulin 1969; Tomita & Shima 1986; Dear & Field 1988*a*; Tomita, Shima & Takayama 1989; Philipp *et al.* 1993; Bourne & Field 1995), the interaction between individual bubbles (Testud-Giovanneshi, Alloncle & Dufresne 1990; Tomita, Sato & Shima 1994) and the collapse of a bubble cluster (Hansson & Mørch 1980; Chahine 1982). Vogel *et al.* (1989) suggested possible mechanisms for jet formation by acoustic transients from adjacent bubbles and/or the change of jet velocity due to deviation from the spherical bubble form which may occur in a fluid flow.

Another important factor influencing the damage of material is the geometry of a boundary surface. It is a familiar finding that in the case of vibratory cavitation the mass loss increases drastically with the lapse of time, particularly after the incubation period, due to the removal of particles from the material surface (Knapp, Daily & Hammitt 1970). Once the material has lost its surface smoothness, the flow field surrounding cavitation bubbles will be affected by the newly formed surface geometry. In particular, the geometry is of great importance to the bubble motion when the surface roughness is comparable to individual bubble sizes. This situation was realized in the erosion experiment by Philipp & Lauterborn (1998) who used 100 identical bubbles and found that the bubble torus disintegrates into many tiny bubbles, each collapsing initially near a flat boundary but later near a non-flat surface due to either plastic deformation of the surface or the loss of material by erosion. When a shock wave is emitted from a bubble near a boundary with a conical depression or with a concave surface, the subsequent reflected shock waves focus near the boundary, producing an even higher pressure which could be a source of a driving force to collapse other bubbles violently (Dear & Field 1988*b*). The high pressure resulting from shock wave focusing has advantages for stone fragmentation during shock wave lithotripsy and recently Zhong *et al.* (1997) developed a more effective method for generating a much higher pressure by making use of a reflector with an adjustable single or double reflecting surface. In this example a spark-induced bubble at the first focus collapses near a concave-shaped boundary of the reflector
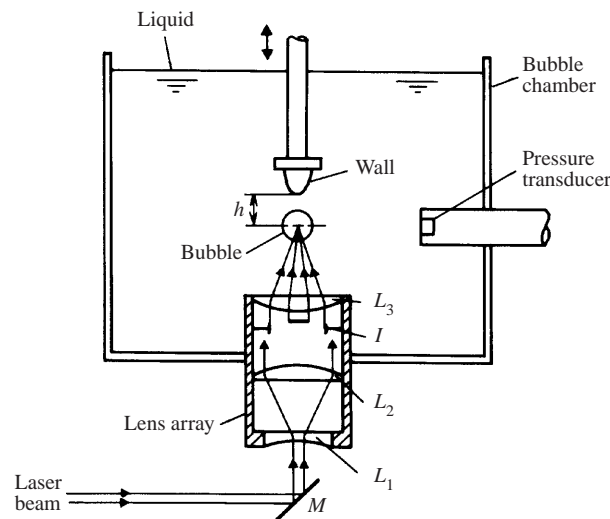
FIGURE 1. Schematic diagram of the experimental arrangement.

accompanied by some migration toward the boundary. Subsequently a shock wave is emitted from the bubble whose location is now nearer the bottom of the reflector, focusing again at around the second focal point of the reflector. To investigate the characteristics of this kind of shock wave focusing, more research is required on the bubble–concave boundary interaction, as pointed out by Tomita *et al.* (1994) in their paper on extracorporeal microexplosion lithotripsy. However, very few studies have been undertaken to date, with exception of Takahira, Fujikawa & Akamatsu (1989), Tomita, Shima & Takahashi (1991) and Tomita, Blake & Robinson (1998).

In this paper, we address the motion of a cavitation bubble near a curved rigid boundary from both a theoretical and experimental perspective. To elucidate the effect of the surface curvature of the boundary, corresponding to the exploration of the influence of a curvature parameter ξ on the bubble motion, an image theory is applied to develop insight into the global bubble motion, and a boundary integral method is employed to investigate the more detailed process of jet formation followed by the toroidal phase of a bubble after jet impact. Numerical calculations are compared with experimental data obtained using laser-induced cavitation bubbles to show the influence of the curvature parameter ξ on the bubble motion.

2. Experimental apparatus and method

Figure 1 is a schematic diagram of the experimental arrangement used to study cavitation bubbles near a curved boundary. Cavitation bubbles were produced on an axial line at a distance L from the apex of the boundary by employing a laser focusing technique which is now standard for realizing a high energy concentration (Lauterborn 1974). A Q-switched ruby laser was used (Japan Sci. Engng. NGP-60MP), delivering light pulses with energy up to 1.2 J with about 20 ns pulse duration, although a low level of energy was required to produce a small bubble (e.g. about 4 mJ for a bubble with 1 mm in radius, Tomita & Shima 1990). To effectively focus the laser beam, a system consisting of three lenses was inserted on the line of the optical axis, in which the laser beam was first expanded by twice the original beam diameter and after collimating it was focused into water with an aspherical convex lens whose focal length was
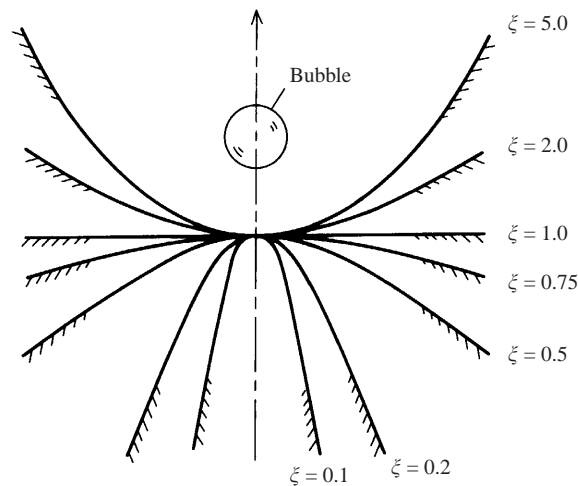
FIGURE 2. The seven wall configurations used in the present experiment.

14 mm in air. To produce a bubble axisymmetrically near a curved wall, the laser beam was focused from the bottom of a bubble chamber (dimensions 240 mm × 240 mm × 300 mm) through a mirror. The curved rigid walls, made of acrylic resin, were created on the free surface side of the apparatus. The shape of the axisymmetric curved walls is specified by the surface parameter ξ which is defined by (1) in §3 obtained from the image theory, giving convex walls when $\xi < 1$, concave walls for $\xi > 1$ and a flat wall when $\xi = 1$. Figure 2 illustrates seven wall configurations used in the present experiment for the case assuming a stand-off parameter $\gamma = 3$. Note that the value of the surface parameter ξ varies with the γ value even when we employ the same boundary. The dynamic motion of cavitation bubbles was recorded using an Imacon high-speed camera (John Hadland 790) primarily with framing rate of 100 000 frames/s and exposure time of 2 μs/frame, together with a Xe flash with a 200 μs pulse duration as the light source. In this case the frame interval was 10 μs. Since the maximum number of frames available to the camera was limited to eighteen, which corresponded to a recording time of 180 μs, the timing for taking high-quality photographs was adjusted with a delay circuit to which the trigger signal was fed from a photocell. Furthermore, we used a higher framing rate of 5 000 000 frames/s only for the purpose of observation of the very early stage of the growth of laser-induced cavitation bubbles. The maximum bubble radius, R_{max}, was directly determined from the photographs obtained, but for bubbles with period longer than 180 μs we indirectly estimated R_{max} from the simultaneously measured pressure versus time curves. Because the time difference between the first two pressure peaks exactly coincides with the period of the motion of a single bubble (Tomita & Shima 1990), the pressure measurement was carried out by a pressure transducer (Kistler Instrumente AG, Switzerland, model 603B, with a 5.55 mm diameter sensitive element, a resonant frequency of 400 kHz, and a rise time of 1 μs) which was positioned 10 mm from the bubble generation.

3. Theory

3.1. *Shape of a curved wall*

A curved wall can be expressed as a steady streamline as a result of the combined flows induced by two point sources with different strengths. As shown in figure 15(*a*)

in the Appendix, if a bubble pulsating at the point $O\,(0,0,h)$ is simulated by a point source with strength $m(=4\pi R^2 \dot{R})$ and the corresponding image with strength $m_A(=\xi^2 m)$ is placed at the point $A\,(0,0,-\xi h)$, we obtain the curved wall as a steady streamline intersecting the axial line at the origin $M\,(0,0,0)$, where $\overline{OM} = h$ and $\overline{MA} = \xi h$. The condition of no flow across the curved wall leads to the following equation with the curvature at the point M being $3(\xi-1)/(4\xi)$ (Takahira *et al.* 1989):

$$\cos\theta_1 - \xi^2 \cos\theta_2 = 1 - \xi^2, \tag{1}$$

where the angles θ_1 and θ_2 are defined in figure 15(*a*) (see the Appendix). Equation (1) determines the shape of a curved wall once ξ is specified. If we instead represent (1) in terms of Cartesian coordinates with $x = r\sin\theta_1 \cos\omega$, $y = r\sin\theta_1 \sin\omega$ and $z = h - r\cos\theta_1$ taking account of the geometric relations on the curved wall surface, we obtain

$$f(x,y,z) = \{x^2 + y^2 + (h-z)^2\}^{1/2}\lfloor\xi^2(z+\xi h) + (1-\xi^2)\{x^2 + y^2 + (z+\xi h)^2\}^{1/2}\rfloor$$
$$-(h-z)\{x^2 + y^2 + (z+\xi h)^2\}^{1/2}$$
$$= 0. \tag{2}$$

Since the bubble position h is initially equal to L, it is clearly seen that the value of ξ must be related to the 'stand-off' parameter γ in order to satisfy (2).

3.2. *Boundary integral method*

We assume for most of the lifetime of a bubble that the liquid surrounding it is inviscid, incompressible and irrotational. The fluid velocity can therefore be represented as the gradient of a potential ϕ which satisfies Laplace's equation.

The boundary integral formulation has become a standard method for simulating the unsteady motion of an ideal fluid bounded by a free surface. It has been particularly successful in predicting aspects of bubble collapse such as the penetration of the liquid jet when a bubble is near a rigid boundary (Blake & Gibson 1987; Blake *et al.* 1993). In integral form, the Laplace equation becomes (Tong *et al.* 1999)

$$\tfrac{1}{2}\phi(x) = \int_{\partial\Omega} \left(\frac{\partial\phi(x')}{\partial n'}G(x,x') - \phi(x')\frac{\partial G(x,x')}{\partial n'}\right)\mathrm{d}\Omega', \tag{3}$$

with x and x' being the position vectors where $x, x' \in \partial\Omega$ (assumed smooth), and $G(x,x') = 1/(4\pi|x - x'|) + |\text{image}|$ is the Green's function consisting of a source and its image in the curved rigid boundary. The normal direction is taken to be outward from the liquid domain (i.e. into the bubble). Up to the time that jet impact occurs, the flow field is simply connected, but upon impact, the flow field becomes doubly connected and thus equation (3) is no longer not valid. To overcome this mathematical difficulty Best (1993) put a cut C across the liquid jet. Velocities on both sides of the cut are equal, but there will be a jump in the potential $\Delta\phi$ corresponding to the circulation around the bubble. The new modified integral equation becomes

$$\tfrac{1}{2}\phi(x) = \int_{\partial\Omega} \left(\frac{\partial\phi(x')}{\partial n'}G(x,x') - \phi(x')\frac{\partial G(x,x')}{\partial n'}\right)\mathrm{d}\Omega' - \Delta\phi\int_C \frac{\partial G(x,x')}{\partial n_+}\mathrm{d}\Omega', \tag{4}$$

where n_+ denotes the normal directed into the liquid on the surface of C away from the rigid boundary. A full description of the method can be found in Best (1993) and related explanations in Blake *et al.* (1998) and Tong *et al.* (1999).

Though the surface tension effect may be important during the late stage of the bubble collapse, it can induce numerical instabilities where there is a loss of

smoothness in the bubble surface and this may finally lead to failure of the calculation. We therefore neglect the surface tension effect when adapting the boundary integral method to the problem under consideration. The liquid pressure at the bubble surface, $p_{r=R}$, is now expressed by

$$p_{r=R} = p_v + p_0 \left(\frac{V_0}{V} \right)^\kappa, \tag{5}$$

where p_v is the vapour pressure of water, p_0 the initial gas pressure and V_0 the initial bubble volume at the time t_0 immediately after the bubble inception, and κ the polytropic index.

The bubble surface and rigid boundary are discretized in a plane through the axis of symmetry and the resulting system of equations is solved for $\partial\phi/\partial n$ on the bubble surface and for ϕ on the curved boundary. This leads to the construction of the free-surface velocities which are used to advance the bubble surface forward in time by means of the kinematic and dynamic boundary conditions written in the following dimensionless form:

$$\frac{\mathrm{D}\boldsymbol{x}^*}{\mathrm{D}\tau} = \nabla\phi^*, \quad \boldsymbol{x}^* \in S_b^*, \tag{6}$$

$$\frac{\mathrm{D}\phi^*}{\mathrm{D}\tau} = \tfrac{1}{2}|\nabla\phi^*|^2 - p^* \left(\frac{V_0}{V} \right)^\kappa + 1, \tag{7}$$

where $\phi^* = \phi/[R_{max}(\Delta p/\rho)^{1/2}]$ with $\Delta p = p_\infty - p_v$, $p^* = p_0/\Delta p$, $\tau = t(\Delta p/\rho)^{1/2}/R_{max}$, $\boldsymbol{x}^* = \boldsymbol{x}/R_{max}$ and $S_b^* = S_b/R_{max}$. Here p_∞ is the ambient liquid pressure, ρ the liquid density, and S_b the bubble surface, and buoyancy effects are neglected for the small bubbles considered here. Finally, $\mathrm{D}/\mathrm{D}\tau$ denotes the material derivative.

For the numerical computations an informed choice must be made for the initial conditions since the bubble contents and rate of expansion near the time of the laser pulse in the experiments are unknown and need to be approximated. Thus the cavitation bubble is assumed to be initially spherical with a dimensionless radius $R_0^*(= R_0/R_{max}) = 0.15742$, which is realized at the dimensionless time $\tau_0 = 0.0034$ from the laser focusing. The initial gas pressure is taken to be $p^* = 100$ as employed by Tong *et al.* (1999) and the polytropic constant $\kappa = 1.33$. The velocity of the bubble surface at the start of the simulation is chosen from energy considerations so that the bubble would attain a maximum radius of 1.0 in a liquid of infinite extent. In the present calculations, a primary concern is to retain similarity between the main features of the bubble shapes in the BIM computation and in the experiment. Therefore the time of the bubble period is not exactly matched between the computation and experiment.

4. Results and discussion

Figure 3(*a*–*e*) shows a series of high-speed photographs, each indicating the overall motion of a bubble near a curved rigid boundary. The photographs were taken with a framing rate of 100 000 frames/s which gives the frame interval of 10 µs and exposure time 2 µs for each frame. Figure 3 covers three categories of boundary configuration: convex boundaries in figure 3(*a*) with $\xi = 0.22$ and $\gamma = 1.2$ ($R_{max} = 0.89$ mm), figure 3(*b*) with $\xi = 0.47$ and $\gamma = 1.5$ ($R_{max} = 0.83$ mm) and figure 3(*c*) with $\xi = 0.72$ and $\gamma = 2.42$ ($R_{max} = 0.78$ mm); a flat boundary in figure 3(*d*) with $\xi = 1.0$ and $\gamma = 1.38$ ($R_{max} = 0.65$ mm); and a concave boundary in figure 3(*e*) with $\xi = 1.19$ and $\gamma = 1.70$ ($R_{max} = 0.75$ mm). On each photograph buoyancy is directed downward, so
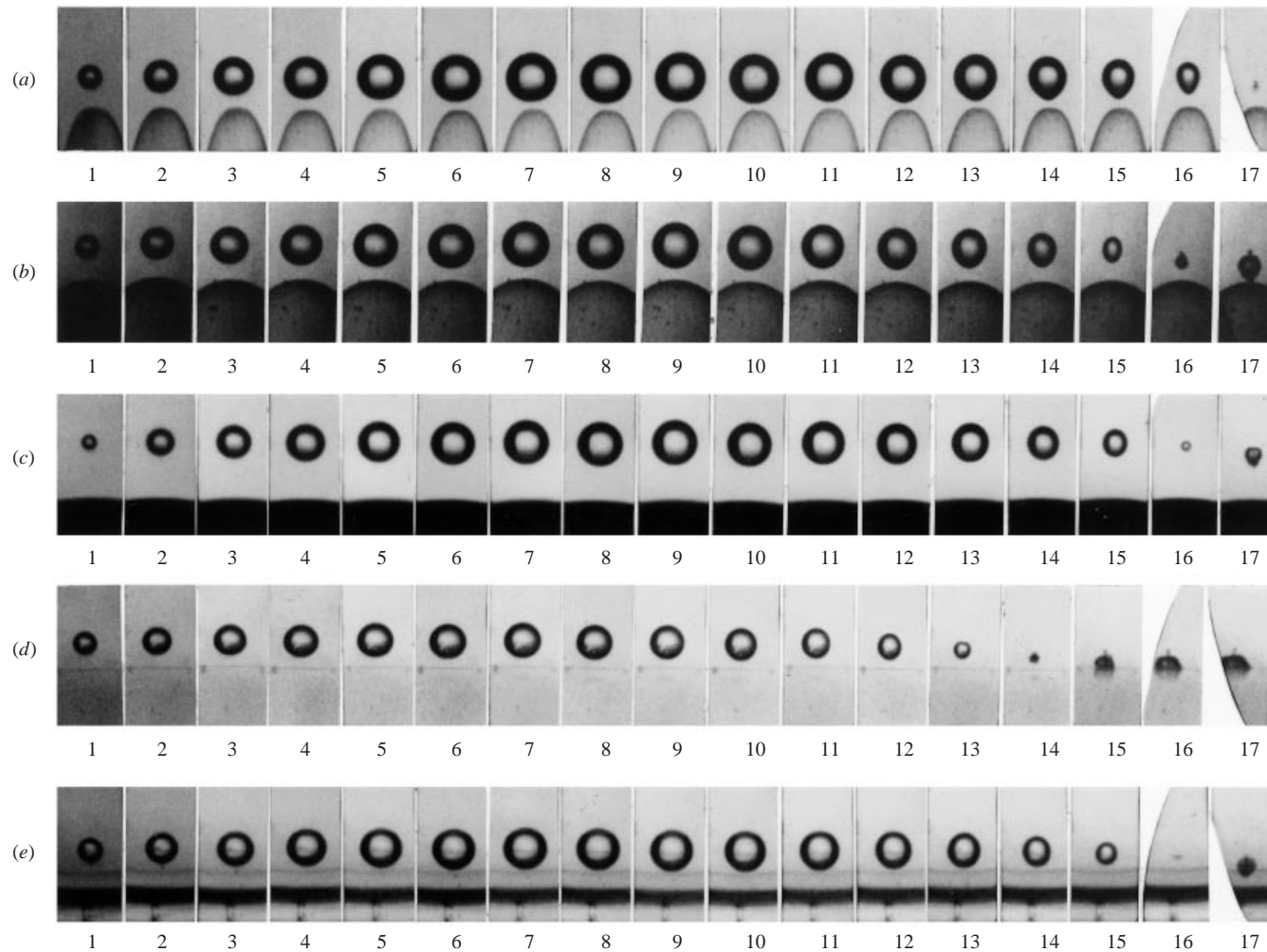
FIGURE 3. High-speed photographs of cavitation bubbles near various curved boundaries; frame interval 10 μs, exposure 2 μs: (a) $\xi = 0.22$, $\gamma = 1.20$ ($R_{max} = 0.89$ mm); (b) $\xi = 0.47$, $\gamma = 1.50$ ($R_{max} = 0.83$ mm); (c) $\xi = 0.72$, $\gamma = 2.42$ ($R_{max} = 0.78$ mm); (d) $\xi = 1.00$, $\gamma = 1.38$ ($R_{max} = 0.65$ mm); (e) $\xi = 1.19$, $\gamma = 1.70$ ($R_{max} = 0.75$ mm).

that both the buoyancy and secondary Bjerknes force are in the same direction. However, the buoyancy is negligible because the bubbles generated in the present experiment are very small. Clearly the bubble motion varies depending not only on the geometry of the nearby boundary (ξ) but also on the initial bubble location from the boundary surface (γ). As the parameter ξ increases, the bubble motion is gradually delayed due to the increased inertance of the nearby boundary which is reflected in the increased strength of the image source in the image system. In fact we can evaluate the bubble period of figure 3(*e*) to be 158 µs which is slightly longer than the bubble period obtained for the flat boundary condition with an identical γ value. In each case of figure 3(*a–e*), a bubble grows almost spherically, but the bubble shape evolves differently during the collapse process: a 'cone-shaped' bubble is formed in the convex wall case, i.e. $\xi < 1$ (see, for example, figure 3*a*) while only a small deviation from the spherical shape can be seen for the concave wall case, i.e. $\xi > 1$ (see figure 3*e*). During the collapse phase of a bubble near a convex boundary, the fluid flow surrounding the bubble converges towards the bubble centre, except for the very narrow region of flow field between the lower bubble surface and the top of the convex boundary where the Bjerknes force is still significant, resulting in a marginal bubble migration toward the boundary. When the curvature of a convex boundary becomes infinite, that is for much smaller ξ, the flow distribution could be similar to that created in the fluid near a conical boundary (Tomita *et al.* 1991) which may produce a self-similar flow distribution by a bifurcation in flow (Peregrine, Shoker & Symon 1990).

Best & Blake (1994) derived the dimensionless period of the bubble motion (i.e. growth and collapse) in the general form

$$\tau_p = \frac{2}{\sqrt{6}} \left\{ B \left(\frac{5}{6}, \frac{1}{2} \right) + \frac{1}{2} \mu B \left(\frac{7}{6}, \frac{1}{2} \right) \right\} = 1.829(1 + 0.4065\mu), \tag{8}$$

where B is an incomplete beta function. The leading term on the right-hand side of (8) is exactly the same as the period of a Rayleigh bubble in an infinite volume of liquid (Rayleigh 1917) and μ is the so-called prolongation coefficient, affected only by the surface geometry of the boundary. Noting that the strength of an image located behind the curved wall at $z^* (= z/R_{max}) = -\xi\gamma$ is $\xi^2 m$, we obtain the coefficient μ as follows:

$$\mu = \frac{\xi^2}{|\boldsymbol{r} - (0, 0, -\xi\gamma)|} = \frac{\xi^2}{\gamma(1 + \xi)}. \tag{9}$$

Since μ increases monotonically with ξ, it is obvious that a convex wall ($\xi < 1$) makes the period of the bubble motion shorter than that obtained in the flat boundary case, while a longer bubble period will be obtained for a concave wall ($\xi > 1$). If we define the distance $L' (= \beta L)$ from the bubble centre to the initial location of a virtual flat wall which has the same effect on the bubble period as a curved wall, the requirement of a flat boundary, i.e. $\mu' = 0.5\gamma'^{-1}$, yields

$$\beta = \frac{1 + \xi}{2\xi^2}. \tag{10}$$

Obviously, the condition $\xi < 1$ leads to $\beta > 1$ where a 'virtual' flat boundary is located far from L, and when $\xi > 1$ we have $\beta < 1$, a closer 'virtual' flat boundary.

To discuss the bubble period more generally, it is useful to explore the motion of a bubble near a sphere because it is one of the most fundamental curved boundaries to study. Figure 4 is a high-speed photograph of the motion of a 0.88 mm bubble generated at the location $L = 1.41$ mm (i.e. $\gamma = 1.6$) from the nearest surface of a
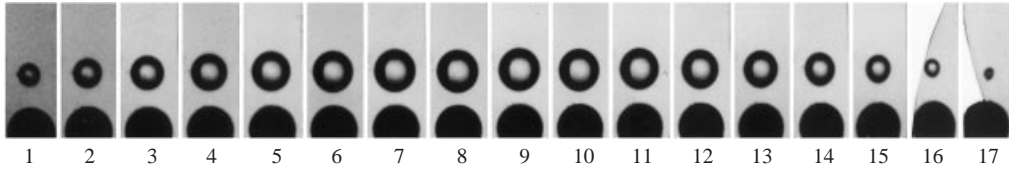
FIGURE 4. Motion of a bubble in the vicinity of a rigid sphere with the radius of 1.0 mm; $\gamma = 1.61$ ($R_{max} = 0.88$ mm), frame interval 10 μs, exposure 2 μs.

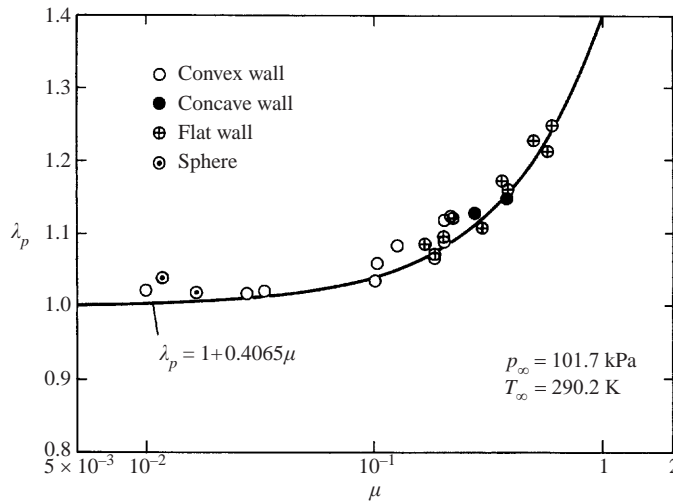FIGURE 5. Period of the bubble motion unified by taking the generalized parameter $\mu = a^*/ \{\gamma(2a^* + \gamma)\} - (1/a^*)\ln[(a^* + \gamma)^2/\{\gamma(2a^* + \gamma)\}]$ for a sphere, and $\mu = \xi^2/\{\gamma(1 + \xi)\}$ for curved boundaries.

sphere with the radius of 1 mm. Similar to the derivation of (9), we can evaluate the coefficient μ for the sphere as follows:

$$\mu = \frac{a^*}{\gamma(2a^* + \gamma)} - \frac{1}{a^*} \ln \left\{ \frac{(a^* + \gamma)^2}{\gamma(2a^* + \gamma)} \right\}, \tag{11}$$

with $a^* = a/R_{max}$ where a is the radius of the sphere. Knowing $a^* = 1.1364$ and $\gamma = 1.6$, we then obtain $\mu = 0.01665$. Since the time interval between the frames of figure 4 is 10 μs, the first period of the bubble oscillation, T_p, can be determined as 165 μs. In dimensionless form, we obtain $\tau_p = 1.8675$. Defining λ_p as the ratio of τ_p to the dimensionless period of a Rayleigh bubble, which is numerically given by 1.829, we finally obtain $\lambda_p = 1.02$. Data measured from the photographs are plotted on figure 5 for several boundary surfaces including convex, concave and flat walls, together with two data points for the sphere including the one mentioned above. In the figure the solid line is the theoretical prediction

$$\lambda_p = 1 + 0.4065\mu, \tag{12}$$

with μ given by (11) for the sphere and by (9) for the curved boundaries (Takahira *et al.* 1989). Good agreement is found between theory and experiment in the examples considered here. On decreasing μ, the value of λ_p tends to approach unity independently of the shape of boundary surface. This is a very reasonable trend because a
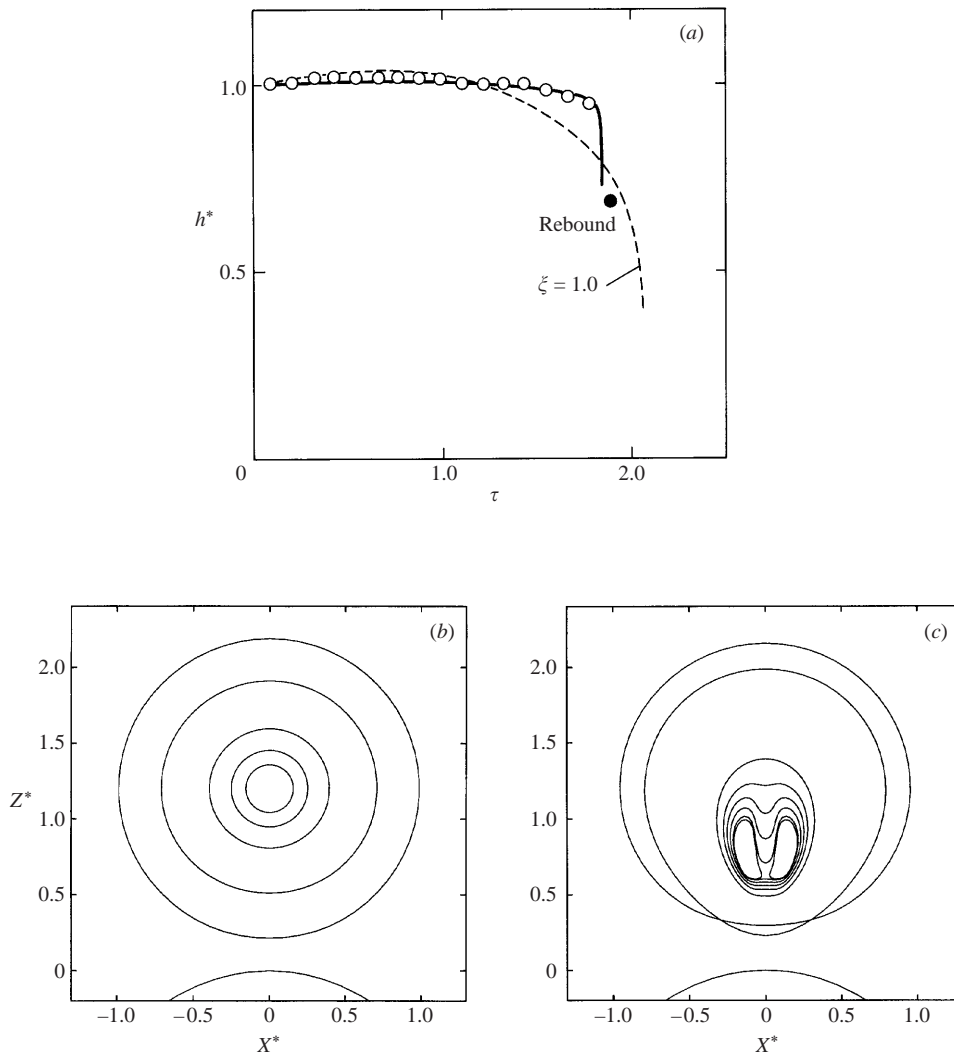
FIGURE 6. Calculated bubble shapes and centroid positions of a bubble near a convex rigid boundary with $\xi = 0.22$ and $\gamma = 1.20$ (i.e. corresponding to figure 3a) are illustrated. (a) Bubble centroid compared to the experimental data denoted by circles, (the solid circle shows a bubble centroid in rebound). (b) Bubble shapes during the growth process and (c) bubble shapes during the collapse process.

smaller μ gives a situation where a bubble oscillates far from the boundary surface, yielding no effective interaction between the bubble and boundary.

Figures 6 and 7 show the characteristic motion of a bubble near a curved rigid boundary for two selected cases, one corresponding to figure 3(a) with $R_{max} = 0.89$ mm, $\gamma = 1.20$ and $\xi = 0.22$, and the other corresponding to figure 3(e) with $R_{max} = 0.75$ mm, $\gamma = 1.70$ and $\xi = 1.19$. In both figures 6 and 7, (a) illustrates the bubble centroid motion and (b) and (c) the bubble shapes changing with time in the growth and collapse phases, respectively. Figure 6(a) shows the bubble centroid versus time curves for $\xi = 0.22$ and $\xi = 1.0$, where the numerical calculations obtained from image theory, which agree well with the solution by the boundary integral method,

are compared with the experimental data denoted by open circles. The solid circle in figure 6(a) corresponds to the centroid of the bubble in rebound. As already observed in figure 3(a), the bubble grows and collapses at almost the same position as the initial one for the whole period of the first bubble oscillation. During a very short time in the late stage of the collapse, the translational motion of the bubble develops as a result of momentum conservation and eventually the bubble rebounds after reaching its minimum volume. This has different characteristics from that of the flat boundary case, i.e. $\xi = 1.0$, shown by a dashed line in figure 6(a) which indicates a marginal migration away from the boundary surface in the growth process followed by a gradual attraction toward the boundary in the collapse process. Furthermore, we notice a significant difference in the bubble period between the $\xi = 0.22$ and $\xi = 1.0$ cases. Obviously, in the $\xi = 0.22$ case the bubble period is much shorter than in the flat boundary case because the nearby boundary modifies the flow field far less, developing weaker pressure gradients (i.e. a weaker image system). Details of the time evolution of the bubble shape can be simulated by the boundary integral method and calculated results are illustrated in figure 6(b) for the growth process and in figure 6(c) for the collapse. As mentioned above, the bubble expands almost spherically throughout the growth process, while during the collapse process it gradually changes its surface configuration, becoming 'cone-shaped '.

A liquid jet is formed at the later stage of the collapse, threading the bubble interior and impacting on the far side of the bubble surface at the elapsed time of $\Delta\tau = 0.0306$ after the jet initiation. The position of the bubble centre at jet penetration can be estimated as $z^*(= z/R_{max}) \approx 0.8$ corresponding to the bubble centroid position $h^*(= h/L) \approx 0.67$ which is close to the experimental point of the bubble centre at the rebound indicated by a solid circle in figure 6(a). The impact velocity of the jet is calculated as $159\,\mathrm{m\,s^{-1}}$ which is about 1.8 times larger than the flat boundary case with the same γ value for a vapour bubble. At jet impact liquid particles near the front of the liquid jet and the lower bubble surface decelerate their forward motion instantaneously. Immediately after the jet impact, the compressible nature of the liquid becomes dominant over a very short interval, causing shock waves to propagate into the flow fields. Consequently a water hammer pressure, approximately evaluated as $\rho c V_{jp}/2$ with c being the sound velocity in liquid, is generated with the peak value equal to $117\,\mathrm{MPa}$, but lasting for an extremely short duration, estimated to be less than $16\,\mathrm{ns}$ since the jet tip radius can be evaluated as $0.0253 R_{max}$. Following the jet impact, complicated flow phenomena will be induced in the form of a pair of vortices and the formation of a splash. These phenomena have recently been investigated using sophisticated computational techniques, and further details may be found in Best (1993), Zhang *et al.* (1993), Blake *et al.* (1998) and Tong *et al.* (1999).

Figure 7 shows the results associated with the concave boundary ($\xi = 1.19$), as recorded in figure 3(e). As mentioned above, this boundary can be regarded as a closer 'virtual' flat boundary and one can confirm this by substituting $\xi = 1.19$ into (10) yielding $\beta = 0.773$ (< 1); the bubble motion is slightly delayed compared to the flat boundary case with $\xi = 1.0$ and $\gamma = 1.70$, designated by a dashed line in figure 7(a). The time evolutions of the bubble growth and collapse in figures 7(b) and 7(c), show that the bubble retains its nearly spherical shape until the early stage of the collapse, but in the final bubble collapse a relatively broad liquid jet is formed. After the jet penetration has been completed, the vortex ring bubble will move toward the bottom of the boundary, and subsequently the second collapse of the bubble will take place in contact with the boundary surface, which is an important situation responsible for cavitation erosion (Philipp & Lauterborn 1998).
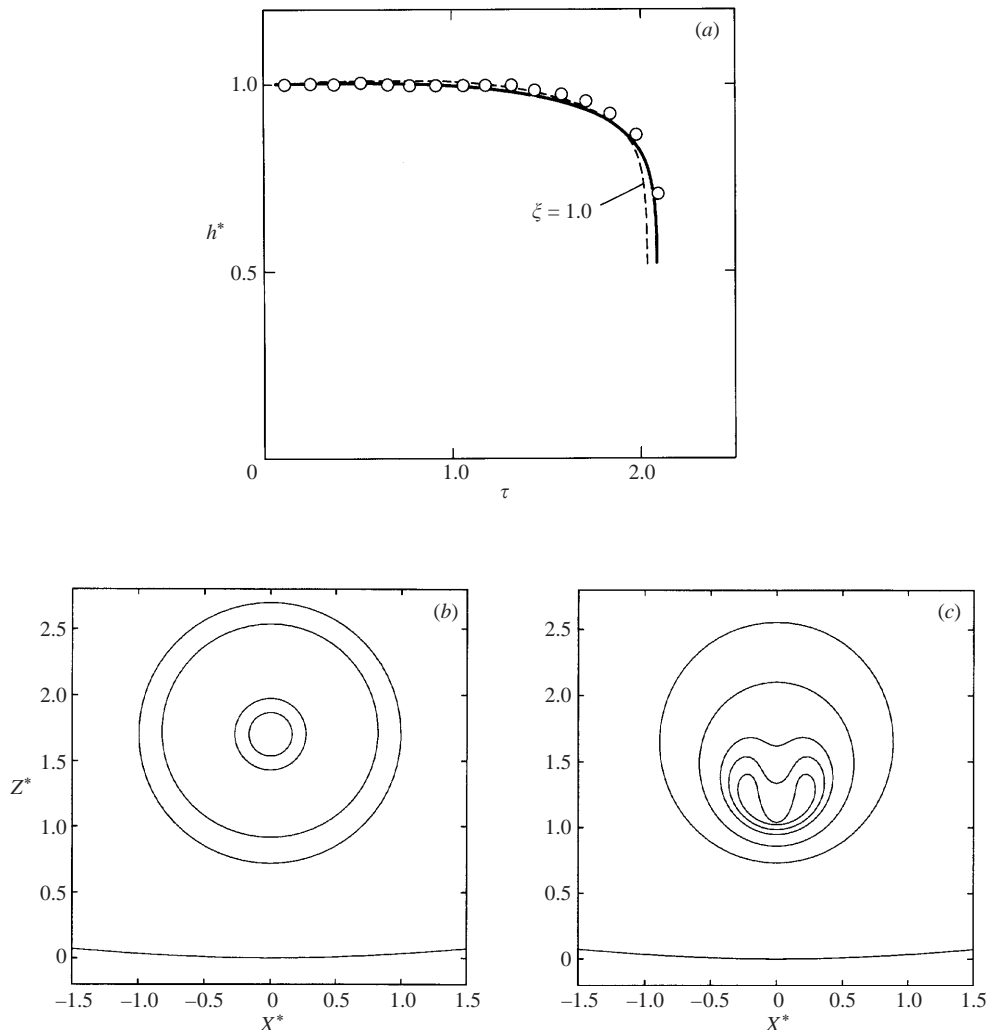
FIGURE 7. As figure 6 but near a concave rigid boundary with $\xi = 1.19$ and $\gamma = 1.70$
(i.e. corresponding to figure 3*e*).

Figure 8 shows a typical example of the motion of a bubble near a convex rigid boundary including the toroidal phase of the bubble. The stand-off parameter was taken to be $\gamma = 1.5$ which is a familiar value often used for the flat boundary case in the literature (Plesset & Chapman 1971; Lauterborn & Bolle 1975; Blake *et al.* 1986). The corresponding experimentally obtained bubble motion is shown in figure 3(*b*) where the curvature parameter is $\xi = 0.47$ and the maximum bubble radius 0.83 mm. The motion of the toroidal stage of the bubble is illustrated in figure 8(*c*), and the growth and collapse processes in figures 8(*a*) and 8(*b*), respectively. The time evolution of bubble growth and collapse is similar to that near a flat rigid boundary with the same γ value. The impact velocity can be determined as 139 m s^{-1}, corresponding to a dimensionless impact velocity of 14, which is 27% larger than that for the flat boundary case (e.g. Blake *et al.* 1986) because of the increased water mass resulting from the boundary configuration being convex. As seen in figure 8(*c*), the toroidal bubble rebounds with a gradual migration toward the apex of the
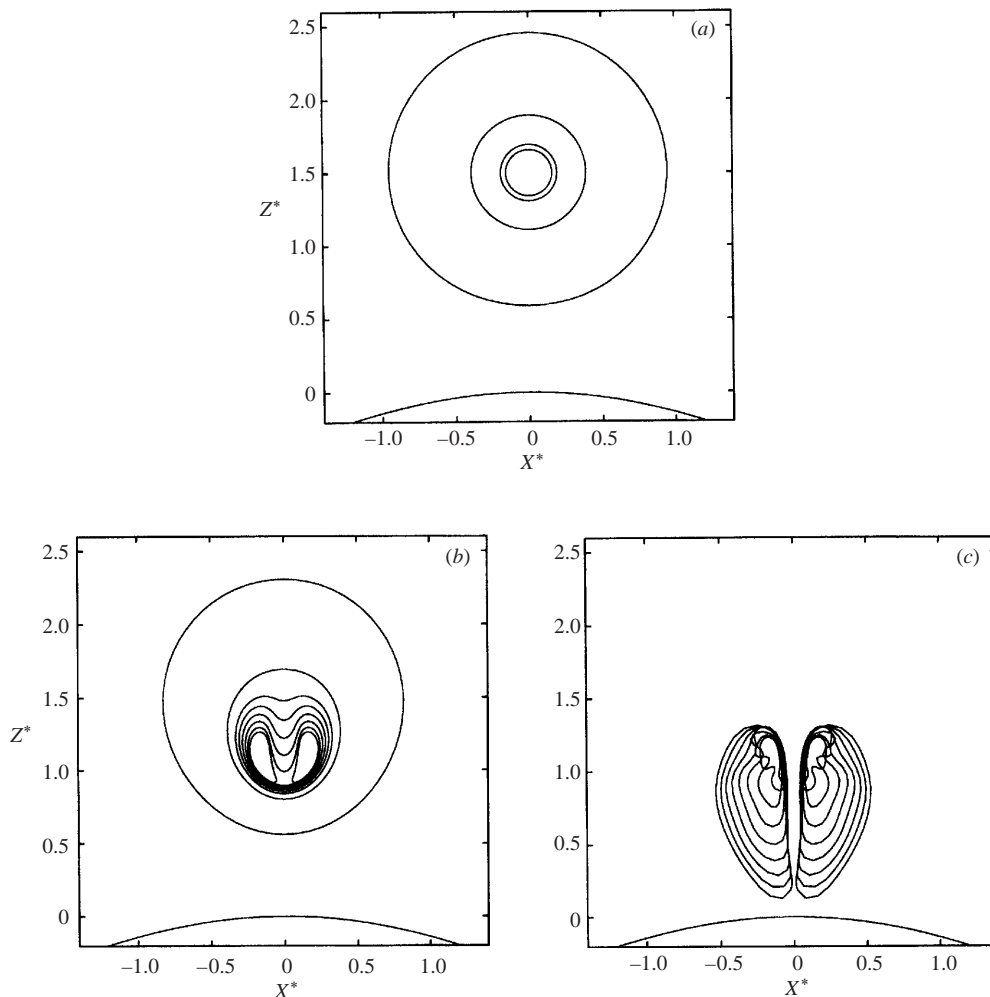
FIGURE 8. Calculated examples of various stages of the bubble motion for a commonly used 'stand-off' parameter, $\gamma = 1.50$, for a bubble near a convex rigid boundary with $\xi = 0.47$ (i.e. corresponding to figure 3b): (a) bubble shapes during the growth process, (b) bubble shapes during the collapse process, and (c) toroidal bubble shapes during the rebound process.

convex boundary producing an elongated shape along the axis of symmetry. In the experiment a counter-jet can be seen, for example in the 16th frame of figure 3(b), in the relatively early stage of the bubble rebound, but the numerical simulation based on the incompressible theory does not capture this phenomenon. This is believed to be due to the compressible nature of liquid during the rebound of the toroidal bubble, which rapidly squeezes a part of the liquid jet, causing a toroidal shock wave. Subsequently a tension wave associated with the reflection of the shock wave from the inner surface of the toroidal bubble occurs and focuses on the axis of symmetry to yield a secondary cavitation like that generated near the bottom of the hump of a rising free surface as reported by Tomita *et al.* (1991). Lindau & Lauterborn (2001) clearly observed the evolution of a counter-jet, disintegrating into a number of tiny bubbles.

Figure 9 illustrates the bubble migration at the minimum bubble volume, defined as
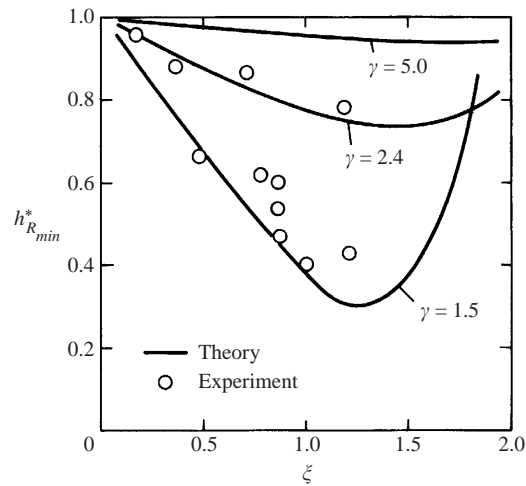
FIGURE 9. Bubble centroid position at the minimum bubble volume is dependent not only on the parameter ξ but also on γ. Maximum bubble migration takes place for $\xi > 1$ which means that the boundary surface is concave.

$h^*_{R_{min}} (= h_{R_{min}}/L)$, versus parameter ξ curves for $\gamma = 1.5$, 2.4 and 5.0. Experimental data for each $h^*_{R_{min}}$ value were determined by interpolation with several data points associated with bubble centroid before/after the minimum bubble volume. The theoretical curves were produced by integrating (A 14) and (A 15) (see the Appendix). A comparison between the theory and experiment indicates a fairly good agreement for $\gamma = 2.4$, but a definite discrepancy is found for $\gamma = 1.5$. A main reason for the discrepancy results from the error in finding the bubble centroid, because the time resolution for photographing the event is insufficient to capture the high-speed phenomena revealed at the final bubble collapse. In addition the image theory loses its validity when γ becomes small. In the region of smaller ξ, corresponding to a boundary with higher curvature, the $h^*_{R_{min}}$ value approaches unity independently of γ owing to the significant reduction in the Bjerknes force. A very interesting feature appears for $\xi > 1$ where the $h^*_{R_{min}}$ curve takes a minimum. This is definite evidence that a slightly depressed boundary surface can attract a bubble quite effectively, and in consequence of this migration the possibility of that the second bubble collapse occurs on the bottom of the concave surface will increase. The position giving the minimum varies with γ, shifting to larger ξ with increasing γ.

It is worth exploring the effect of the geometry of a boundary surface on the impact velocity of a liquid jet, since it is regarded as one of the important factors in cavitation damage. In relation to the erosion problem, a particularly relevant situation is where a vapour bubble is in contact with the boundary surface (i.e. $\gamma = 1$) because this is very close to the situation where the maximum jet damage could be achieved because the jet impact on the boundary can occur at the moment of minimum bubble volume (Kling & Hammitt 1972). Therefore, taking $\gamma = 1$, numerical calculations were carried out by using the boundary integral method. To elucidate the effect of ξ on the impact velocity of a liquid jet formed inside a vapour bubble, the calculations were conducted to obtain the jet impact velocity which is normalized with that obtained for the flat boundary case, i.e. $V^*_{jp} (= V_{jp}(\xi)/V_{jp}(\xi = 1))$. The calculated results are plotted against ξ on figure 10 as a curved solid line, with a dashed line in the region $\xi < 0.4$ where a liquid jet directed away from the boundary is formed under some conditions.
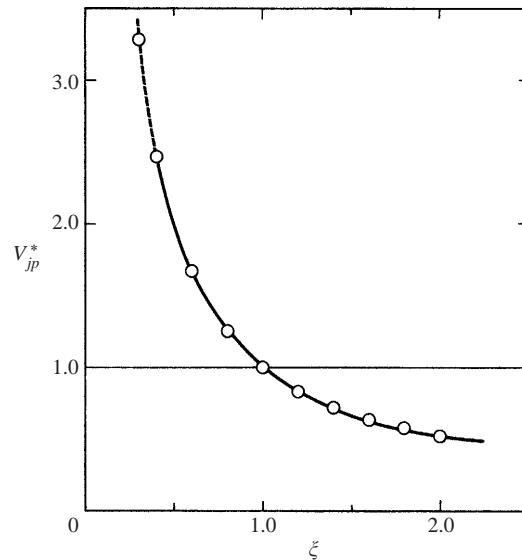
FIGURE 10. Effect of the parameter ξ on the liquid jet velocity for the case $\gamma = 1.0$. When a vapour bubble collapses near a convex boundary (i.e. $\xi < 1$), especially for high wall curvature, the jet velocity is much higher than that of the flat boundary case. The dashed line for $\xi < 0.4$ shows the region where a collapsing bubble tends to detach from the boundary to form a liquid jet directed away from the boundary. However the formation of this kind of liquid jet is very sensitive to the initial conditions.

Obviously there exists a region of $V_{jp}^* > 1$ when $\xi < 1$ where the jet impact occurs on the top of the boundary surface and its velocity always exceeds the jet velocity achieved from the bubble in contact with a flat boundary, i.e. $V_{jp}(\xi = 1)$. However in the region $\xi < 0.4$, a collapsing bubble tends to detach from the boundary to form a liquid jet directed away from the boundary. When $\xi = 0.4$, we obtain a V_{jp}^* value that is 2.47 times larger than that for $\xi = 1$. On the other hand, the jet impact velocity in the region $\xi > 1$ is always below the value of $V_{jp}(\xi = 1)$. As a result, when a boundary surface becomes rough due to exposure to cavitation for a long time, smaller bubbles can collapse intensively, producing much higher liquid jets velocities and impact pressures. This model of high pressure generation seems to be important and may be realized very often in real situations.

As mentioned above, we should note that a significant feature appears on the bubble surface for a boundary with small ξ. The calculations indicate the formation of a liquid jet directed away from the boundary when ξ is less than 0.4. Figure 11 is an example of a calculation for $\xi = 0.2$ for almost the same conditions used in the experiment of figure 12(a) below, except that, in the latter case, the bubble initial location is closer to the boundary and the bubble becomes attached during the collapse. The bubble surface shapes are very similar for the calculation and experiment, excepting the evidence of the bubble detachment which occurs in the calculation during the later stage of the collapse where the inflow induced along the boundary leads to the liquid jet formation originating from the bubble surface closest to the boundary and directed away from the boundary. This opposing jet forms before the formation of a liquid jet towards the boundary and there is an impact of the two jets inside the bubble. However, the formation of a jet away from the boundary is very sensitive to the initial conditions. In certain cases there is a slowing of the
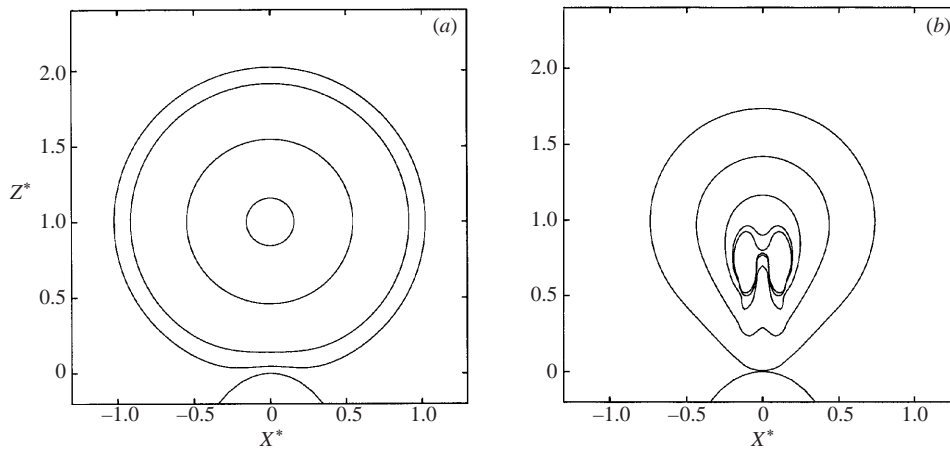
FIGURE 11. Two liquid jets form in opposite directions during the collapse of a bubble close to a convex boundary with the conditions $\xi = 0.2$ and $\gamma = 1.0$: (a) bubble shapes during growth; (b) bubble shapes during collapse.

initial jet away from the boundary and then jetting in a ring around this first jet, still directed away from the boundary, but followed by a jet towards the boundary. For $\xi < 0.2$, the opposing jet begins to form but is more like an irregularity in the surface as the bubble continues to collapse.

When a bubble collapses when attached to a convex boundary, several modes of collapse can be observed. Figures 12–14 show five examples of high-speed photographs indicating the collapse of bubbles attached to two kinds of convex boundaries, which are the same as those in figures 3(a) and 3(b), subsequently followed by the rebound processes. Figure 12(a) is the case with $\xi = 0.19$ and $\gamma = 0.95$ ($R_{max} = 1.08$ mm) where a bubble begins to collapse when almost in contact with the apex of the curved boundary, and the shape of the bubble surface closer to the boundary gradually changes into a 'cone-shape' due to the pressure gradient induced by an inward flow along the curved boundary. During the last stage of the collapse the opposite bubble surface further from the boundary becomes flat, causing a high-speed axial liquid jet directed towards the boundary. Figure 12(b) corresponds to the motion of a smaller bubble with $\xi = 0.26$ and $\gamma = 0.28$ ($R_{max} = 0.82$ mm). A notable feature can be seen in this case: the bubble shape becomes slightly oblate when it reaches its maximum volume. During the early stage of the collapse the contraction proceeds at almost the same rate over all the bubble surface. However in the later stage of the collapse, a difference appears on the portion of the bubble closest to the boundary which collapses faster than the opposite bubble surface. In the 4th frame a counter-jet-like projection can be seen on the axis of symmetry, but no bubble separation occurs. After the rebound ceases, the slender projection and the attached bubble again collapse with different time scales. These observations indicate two features; one associated with the liquid jet formation during the final stage of the bubble collapse, remaining as a black line inside the attached bubble during its rebound process; the other concerned with the slender projection which is a secondary cavity because it behaves differently from the main bubble, reaching a minimum volume during the 11th and 12th frames and then rebounding. The change of the bubble surface with the lapse of time, especially the curvature variation, is clearly seen in the series of enlarged pictures of figure 13 where the conditions are $\xi = 0.25$ and $\gamma = 0.22$ ($R_{max} = 1.57$ mm). The
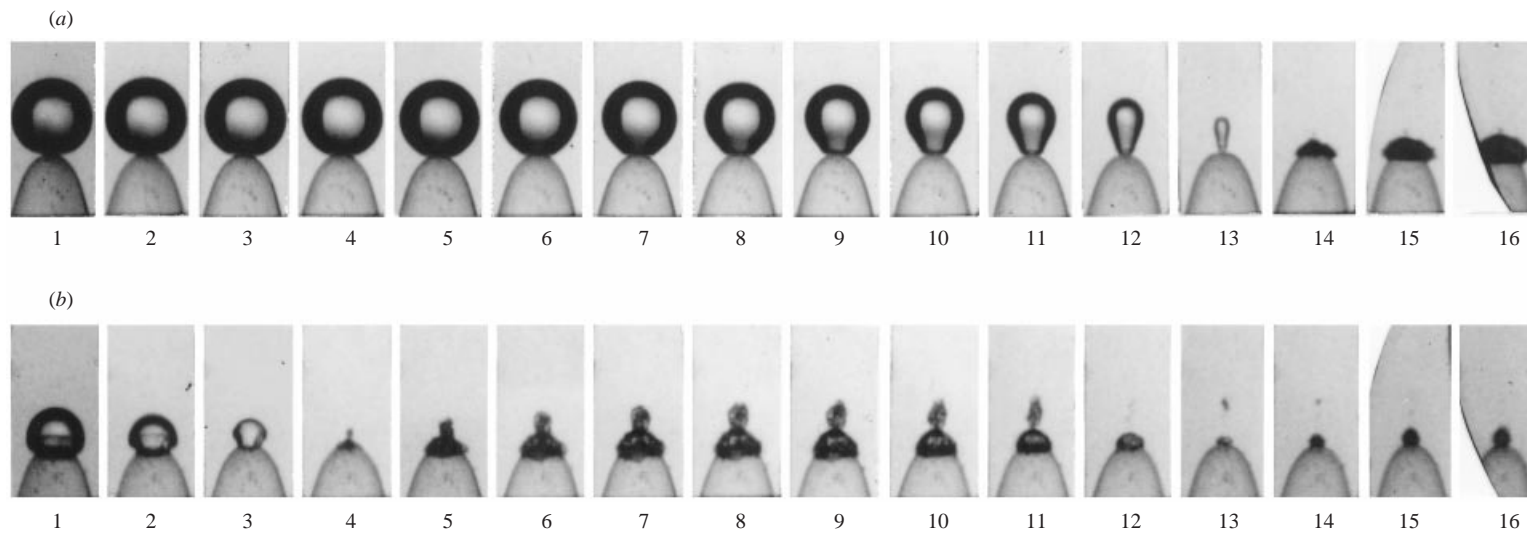
FIGURE 12. Collapse process and the subsequent motion of cavitation bubbles attached to a curved boundary identical with that used in figure 3(*a*), frame interval 10 μs, exposure 2 μs: (*a*) $\xi = 0.19$, $\gamma = 0.95$ ($R_{max} = 1.08$ mm); (*b*) $\xi = 0.26$, $\gamma = 0.28$ ($R_{max} = 0.82$ mm).
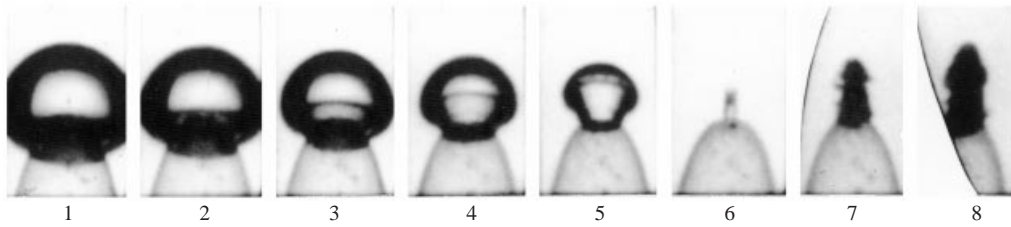
FIGURE 13. Pronounced deformation of the surface of a cavitation bubble attached to a curved boundary, which is identical with that used in figure 3(a), with the conditions $\xi = 0.25$ and $\gamma = 0.22$ ($R_{max} = 1.57$ mm); frame interval 10 μs, exposure 2 μs.
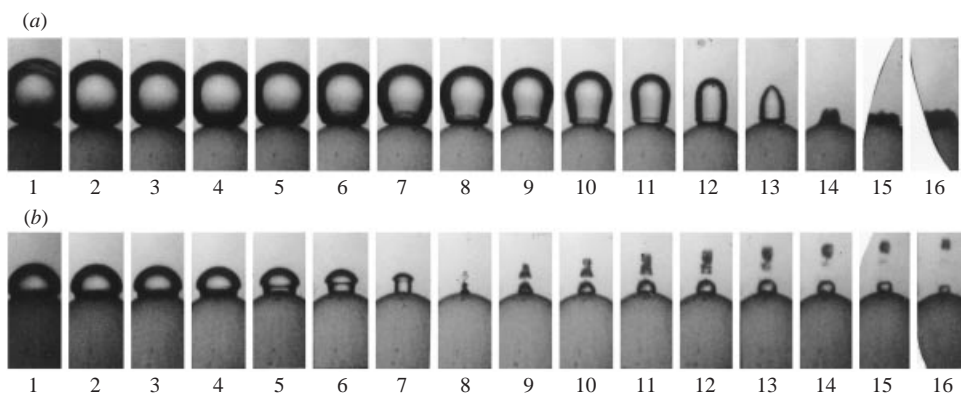

FIGURE 14. Interaction of an attached bubble with a convex boundary, which is identical with that used in figure 3(b). In (a) with the conditions of $\xi = 0.18$, $\gamma = 0.87$ ($R_{max} = 1.47$ mm), the jet impact with the boundary is a significant feature but no bubble separation occurs. In (b) with $\xi = 0.65$, $\gamma = 0.33$ ($R_{max} = 1.05$ mm), a strong interaction results in the bubble separation: frame interval 10 μs, exposure 2 μs.

highest-curvature region moves faster towards the opposite bubble surface. The 6th frame shows the bubble behaviour immediately before its collapse point, indicating a much smaller cylindrical shape accompanied by a black spot at the top which is a very fine liquid jet directed downwards with a velocity of 103 m s^{-1} averaged between the 5th and 6th frames.

Figure 14 shows two sets of high-speed photographs indicating the motion of a bubble attached to the same convex boundary as in figure 3(b). Figure 14(a) corresponds to the conditions of $\xi = 0.18$ and $\gamma = 0.87$ ($R_{max} = 1.47$ mm) where a bubble is attached to the boundary surface when it reaches maximum volume. During the collapse process, the bubble becomes elongated in the direction of the axis of symmetry due to momentum conservation. No bubble separation occurs; instead a sharp edge can be seen on the opposite bubble surface in the 13th frame, leading to the liquid jet formation. On the other hand, figure 14(b) corresponds to the conditions $\xi = 0.65$ and $\gamma = 0.33$ ($R_{max} = 1.05$ mm) with the bubble shape being oblate at its maximum volume. A mushroom-like bubble is formed, changing its configuration drastically during the later stage of the collapse. An inward flow along the curved boundary pushes up the cap of the bubble from below to promote the elongation of the neck of the mushroom-like bubble. Because of the higher curvature at the cap, it collapses faster than the other parts of the bubble surface resulting in the production of a radial jet flow. In the 8th frame, bubble separation occurs, creating

two smaller bubbles. After the separation has been completed, a newly created attached bubble expands on the boundary surface and then shrinks. This may be one mechanism responsible for bubble proliferation. Furthermore, we can observe a protrusion appearing on the surface of the second bubble separated from the original bubble, which extends away from the boundary due to the vertical flow along the curved boundary. The mechanism of protrusion formation in the separated smaller bubble is due to the high curvature at the separated edges of the bubble surfaces, followed by a very fine microjet with higher velocity. This phenomenon observed after the 9th frame is very similar to that reported elsewhere (Lauterborn & Hentschel 1985).

When a bubble collapses attached to a flat boundary we observed neither bubble separation nor the pinch-off phenomenon within the limits of the present experiment. For a boundary with an even slightly convex shape, however, a pinch-off phenomenon occurred. Consequently we conclude that an important factor in the generation of bubble separation is the bubble shape being oblate at its maximum volume. In fact there are several experimental results regarding bubble separation. For instance, Tomita & Shima (1990) found a mushroom-like shape of the bubble surface when a bubble collapses attached to a rubber surface, followed by pinch-off. More recently Brujan *et al.* (2001) carried out a very sophisticated experiment on the dynamics of bubbles near a PAA boundary and showed that bubble separation occurred when the bubble shape at its maximum volume was oblate. Similar evidence was obtained by Tomita & Kodama (2001) for the case where two different sized laser-induced cavitation bubbles were in the vicinity of a free surface. When a smaller bubble located far from the free surface reaches its maximum volume with an oblate shape, it collapses, while a larger bubble still continues to grow. In the later stage of the collapse of the smaller bubble, it becomes mushroom-shaped, resulting in the separation into two parts into much smaller bubbles which migrate in opposite directions.

5. Concluding remarks

The motion of a cavitation bubble near a curved rigid boundary has been investigated in detail. Experimentally, the motion of laser-induced cavitation bubbles was followed by using high-speed photography. On the theoretical side, two methods were applied to gain general knowledge about bubble motion near a curved boundary, one utilizing the image theory to explore the effect of a parameter ξ on the bubble centroid and the other the boundary integral method to obtain detailed features of bubble shape with the lapse of time, including liquid jet formation. Theoretical predictions show a favourable agreement with the experimental data, especially with regard to the bubble centroid motion and the bubble period for the first oscillation. The bubble period is formulated in more unified form by introducing a generalized variable, indicating that it becomes shorter when a boundary is convex while a concave wall makes it longer. The most pronounced migration takes place when a boundary is slightly concave, which is completely different to the convex boundary case where a drastic suppression of translational bubble motion is evident. The velocity of a liquid jet impacting on the boundary surface tends to increase with decreasing ξ, becoming larger compared to the flat boundary case when $\xi < 1$. For instance in the case of $\xi = 0.4$, the jet velocity attained could be nearly two and a half times larger than the flat boundary result. The results obtained here partly explain existing experimental findings that indicate a rapid increase in mass loss appearing after an incubation period of vibratory cavitation erosion.
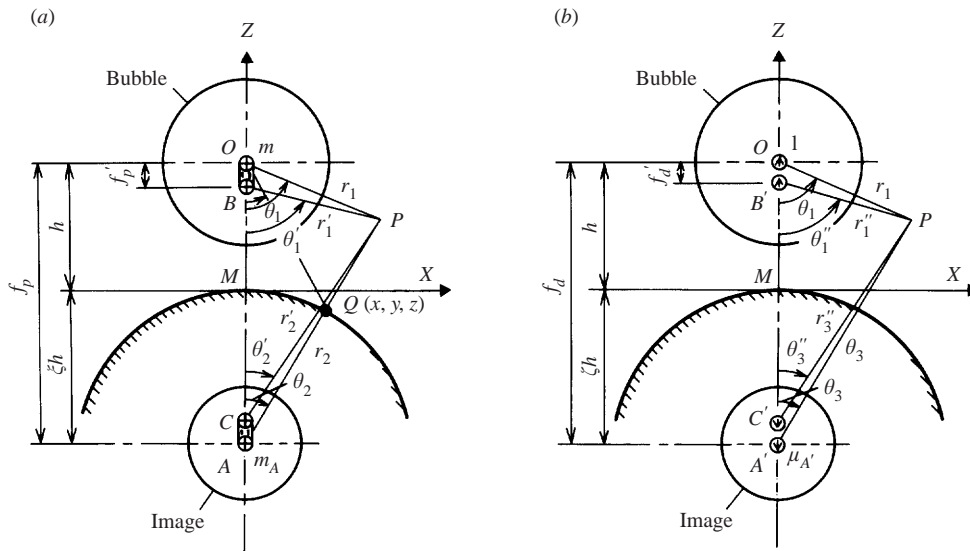
(*a*)

(*b*)

FIGURE 15. Image systems for (*a*) bubble pulsation and (*b*) translational bubble motion.

In conclusion the surface roughness of a boundary must be one of the essential factors in promoting cavitation erosion. Bubble separation occurs when a bubble, which is oblate at maximum volume, collapses while attaching to a convex boundary surface, followed by bubble splitting, which may be responsible for bubble proliferation.

Appendix

The global bubble motion can be simulated by introducing a series of images (Cole 1948). The radial bubble motion requires a combination of point sources and line sinks and their images which are positioned at a distance ξh behind a point M as shown in figure 15(*a*). In a similar manner, as indicated in figure 15(*b*), the translational bubble motion can be simulated using dipoles and their images which are positioned at a distance ζh behind point M in order to satisfy the boundary condition on the curved wall, where ζ is a function of ξ. The potential ϕ of the whole system is now given by

$$\phi = \dot{R}\phi^r + \dot{h}\phi^z, \tag{A 1}$$

with $\dot{R} = \mathrm{d}R/\mathrm{d}t$ and $\dot{h} = \mathrm{d}h/\mathrm{d}t$ where R is the bubble radius at time t and h the distance from the bubble centre to the origin M at time t. In addition, ϕ^r and ϕ^z represent the unit velocity potentials for radial and translational components which each satisfy Laplace's equation with the boundary conditions

$$\frac{\partial \phi^r}{\partial n} = -1, \quad \frac{\partial \phi^z}{\partial n} = -\cos\theta \tag{A 2}$$

on the bubble surface, and those on the curved rigid boundary given by

$$\frac{\partial \phi^r}{\partial n} = 0, \quad \frac{\partial \phi^z}{\partial n} = 0. \tag{A 3}$$

The kinetic energy of the liquid surrounding a bubble can be expressed in terms of the velocity potentials ϕ^r and ϕ^z as follows (Milne-Thomson 1968):

$$T = \frac{\rho}{2} \left\{ \dot{R}^2 \int_S \int \phi^r \, dS + 2\dot{R}\dot{h} \int_S \int \phi^z \, dS + \dot{h}^2 \int_S \int \phi^z \cos\theta \, dS \right\}. \tag{A 4}$$

Within the limit of the first-order correction in the flow field, we finally obtain the kinetic energy of the liquid in the following form:

$$T = 2\pi\rho(1 + f_0)R^3\dot{R}^2 - 4\pi\rho f_1 R^3\dot{R}\dot{h} + \frac{\pi\rho}{3}(1 + 3f_2)R^3\dot{h}^2, \tag{A 5}$$

where

$$f_0 = \frac{\xi^2 R}{h(1 + \xi)} + \frac{\xi^4 R^2}{h^2(1 + \xi)^2 - \xi R^2} - \xi^4 \ln\left\{ \frac{h^2(1 + \xi)^2}{h^2(1 + \xi)^2 - \xi R^2} \right\}, \tag{A 6}$$

$$f_1 = \frac{\zeta^3}{2} \left\{ \frac{R}{h(1 + \zeta)} \right\}^2 \left[1 + \eta^3 \left\{ \frac{R^3}{h^3(1 + \zeta)(1 + \eta)^2} \right\} \right], \tag{A 7}$$

$$f_2 = \frac{\zeta^3}{3} \left\{ \frac{R}{h(1 + \zeta)} \right\}^3 \left[3 + 2\eta^3 \left\{ \frac{R}{h(1 + \eta)} \right\}^3 \right]. \tag{A 8}$$

The variables ζ and η in (A 7) and (A 8) are functions of ξ, relating to a series of dipole sources and their images. To form a curved boundary the following relation between the angles θ_1 and θ_3 is required:

$$\sin\theta_1 = \zeta \sin\theta_3, \tag{A 9}$$

which must satisfy (1).

Derivation of $\zeta = \zeta(\xi)$ for $\zeta \leqslant 1$

Since (1) and (A 9) must be satisfied at the arbitrary point Q on the convex boundary surface, when we take $\theta_2 = \pi/2$, we obtain

$$\zeta = \frac{1}{(2 - \xi)}\{-(1 - \xi)^2 + \sqrt{(1 - \xi)^4 + \xi(2 - \xi)(3 - 2\xi)}\}, \tag{A 10}$$

which yields $\zeta = 1$ when $\xi = 1$ and $\zeta = 0$ when $\xi = 0$.

Derivation of $\zeta = \zeta(\xi)$ for $\zeta \geqslant 1$

When $\theta_1 = \pi/2$ and dealing with the relations in a similar manner to the above, we obtain

$$\zeta = \frac{\xi(3\xi - 2)}{(\xi^2 + 2\xi - 2)}, \tag{A 11}$$

which gives $\zeta = 1$ when $\xi = 1$ and asymptotes to $\zeta \to 3$ when $\xi \to \infty$. Although the difference between the configurations of a curved wall expressed by (1) and by (A 9) becomes evident in the region $\theta_2 > \pi/2$ for $\xi < 1$ and $\theta_1 > \pi/2$ for $\xi > 1$, a very good agreement between them is found in the range $0 \leqslant \theta_3 \leqslant \pi/2$. The variable η is a function of ξ and ζ, which can be determined in a similar manner to the derivations of (A 10) and (A 11).

Because buoyancy effects are negligible when the bubble is small, the bubble internal energy E can be expressed as

$$
\begin{aligned}
E(R) &= -\int_R^\infty (p_{r=R} - p_\infty)\,\mathrm{d}V \\
&= \frac{4\pi R^3}{3}\left[p_\infty - p_v - \frac{p_0}{(1-\kappa)}\left(\frac{R_0}{R}\right)^{3\kappa} + \frac{3\sigma}{R} \right]
\end{aligned}
\tag{A 12}
$$

provided the gas contents inside the spherical bubble obey a polytropic law and where $p_{r=R}$ is the liquid pressure at the bubble surface given by

$$
p_{r=R} = p_v + p_0\left(\frac{R_0}{R}\right)^{3\kappa} - \frac{2\sigma}{R}.
\tag{A 13}
$$

In the above expression, R_0 is the initial bubble radius at time t_0 and σ the surface tension of the liquid. We, therefore, determine the simultaneous ordinary differential equation of motion of a bubble by applying the method of Lagrange. This leads to the following equations for the bubble radius R and the translational displacement h as generalized:

$$
\begin{aligned}
\ddot{R} = \frac{-1}{R(1+f_0+3f_2+3f_0f_2-6f_1^2)} \\
\times \Bigg\{ \tfrac{3}{2}\dot{R}^2\left[(1+3f_2)\left(1+f_0+\frac{R}{3}f_{0,R}\right) - 2f_1(6f_1+Rf_{0,h}+2Rf_{1,R}) \right] \\
+ \dot{R}\dot{h}[R(1+3f_2)f_{0,h}+3f_1(1+3f_2+Rf_{2,R})] \\
- \frac{\dot{h}^2}{4}[(1+3f_2)(1+3f_2+4Rf_{1,h}+Rf_{2,R})-6Rf_1f_{2,h}] \\
- \frac{(1+3f_2)}{\rho}\left[p_v + p_0\left(\frac{R_0}{R}\right)^{3\kappa} - \frac{2\sigma}{R} - p_\infty \right] \Bigg\},
\end{aligned}
\tag{A 14}
$$

$$
\begin{aligned}
\ddot{h} = \frac{-1}{R(1+f_0+3f_2+3f_0f_2-6f_1^2)} \\
\times \Bigg\{ \tfrac{3}{2}\dot{h}^2[R(1+f_0)f_{2,h}-f_1(1+3f_2+4f_{1,h}+Rf_{2,R})] \\
+ 3\dot{R}\dot{h}[(1+f_0)(1+3f_2+Rf_{2,R})+2Rf_1f_{0,h}] \\
- 3\dot{R}^2[(1+f_0)(3f_1+Rf_{0,h}+2Rf_{1,R})-Rf_1f_{0,R}] \\
- \frac{6f_1}{\rho}\left[p_v + p_0\left(\frac{R_0}{R}\right)^{3\kappa} - \frac{2\sigma}{R} - p_\infty \right] \Bigg\},
\end{aligned}
\tag{A 15}
$$

where

$$
\left.
\begin{aligned}
f_{0,R} &= \frac{\partial f_0}{\partial R}, \quad f_{0,h} = \frac{\partial f_0}{\partial h}, \\
f_{i,R} &= \frac{\partial f_i}{\partial R} + \left(\frac{\partial f_i}{\partial \eta}\right)\left(\frac{\partial \eta}{\partial R}\right), \quad f_{i,h} = \frac{\partial f_i}{\partial h} + \left(\frac{\partial f_i}{\partial \eta}\right)\left(\frac{\partial \eta}{\partial h}\right) \quad (i=1,2).
\end{aligned}
\right\}
\tag{A 16}
$$

Equations (A 14) and (A 15) can be solved numerically by means of the Runge–

Kutta–Gill method with the following initial conditions:

$$R_0^* = 0.1, \quad \dot{R}_0^* = \left[\frac{2(R_0^{*^{-3}} - 1)}{3 \left\{ 1 + \dfrac{\xi^2 R_0^*}{\gamma(1 + \xi)} \right\}} \right]^{1/2}, \\ h_0^* = 1.0, \quad \dot{h}_0^* = 0. \tag{A 17}$$

In (A 17), $R_0^* = R_0/R_{max}$, $h_0^* = h_0/L$ with h_0 being the initial distance from the bubble centre to the boundary surface $(\equiv L)$. Furthermore $\dot{R}_0^*$ is the initial velocity of the radial motion of a Rayleigh bubble modified by including the wall effect as expressed in the second term in the denominator, which can be readily derived by integrating (A 19) below.

From observations of the very early stage of the growth of laser-induced cavitation bubbles using the framing rate of $5\,000\,000$ frames/s, the time giving the initial bubble radius specified in (A 17) is estimated to be $\tau_0 = 0.0012$ from the plasma luminescence. Although the initial laser-induced bubble is not spherical but somewhat elongating along the optical axis, which is coincident with the symmetric axis of the curved walls, we experimentally found that some time after the plasma formation, i.e. $\tau > \tau_0$, the change of the bubble volume with time gave almost the same results for the experiment and a Rayleigh bubble (Tomita *et al.* 2000). It is also reasonable to assume that a laser-induced cavitation bubble contains both vapour and some non-condensable gases, probably produced by the dissociation of the water molecules and/or those existing inside the volume of a plasma dissolved as cavitation nuclei. In the calculation κ is taken as $4/3$. In (A 14) and (A 15), taking $\xi = 1$ and $\zeta = 1$ easily leads to the equations of motion of a bubble near a flat boundary (Tomita *et al.* 1992; Sato, Tomita & Shima 1993).

When taking no account of translational bubble motion $(\dot{h} = 0, \ddot{h} = 0)$ and providing no correction for the flow field induced by an image source, the velocity potential becomes

$$\phi^r = R^2 \left(\frac{1}{r_1} + \frac{\xi^2}{r_2} \right), \tag{A 18}$$

with r_1 and r_2 being the distances from the bubble centre to the point P in the liquid and its image centre to the point P, respectively. Assuming that the effect of the surface tension on the bubble motion is negligibly small and the bubble contains only vapour we, therefore, obtain the equation of radial motion of a vapour bubble near a curved wall as follows:

$$R\ddot{R} \left\{ 1 + \frac{\xi^2 R}{L(1 + \xi)} \right\} + \tfrac{3}{2} \dot{R}^2 \left\{ 1 + \frac{4\xi^2 R}{3L(1 + \xi)} \right\} + \frac{\Delta p}{\rho} = 0, \tag{A 19}$$

which coincides with the equation developed by Takahira *et al.* (1989).

REFERENCES

BENJAMIN, T. B. & ELLIS, A. T. 1966 The collapse of cavitation bubbles and the pressures thereby produced against solid boundaries. *Phil. Trans. R. Soc. Lond.* A **260**, 221–240.

BEST, J. P. 1993 The formation of toroidal bubbles upon the collapse of transient cavities. *J. Fluid Mech.* **251**, 79–107.

BEST, J. P. & BLAKE, J. R. 1994 An estimate of the Kelvin impulse of a transient cavity. *J. Fluid Mech.* **261**, 75–93.

BLAKE, J. R. & GIBSON, D. C. 1987 Cavitation bubbles near boundaries. *Annu. Rev. Fluid Mech.* **19**, 99–123.

BLAKE, J. R., ROBINSON, P. B., SHIMA, A. & TOMITA, Y. 1993 Interaction of two cavitation bubbles with a rigid boundary. *J. Fluid Mech.* **255**, 707–721.

BLAKE, J. R., TAIB, B. B. & DOHERTY, G. 1986 Transient cavities near boundaries. Part 1. Rigid boundary. *J. Fluid Mech.* **170**, 479–497.

BLAKE, J. R., TOMITA, Y. & TONG, R. P. 1998 The art, craft and science of modeling jet impact in a collapsing cavitation bubble. *Appl. Sci. Res.* **58**, 77–90.

BOURNE, N. K. & FIELD, J. E. 1995 A high-speed photographic study of cavitation damage. *J. Appl. Phys.* **78**, 4423–4427.

BRUJAN, E.-A., NAHEN, K., SCHMIDT, P. & VOGEL, A. 2001 Dynamics of laser-induced cavitation bubbles near an elastic boundary. *J. Fluid Mech.* **433**, 251–281.

CHAHINE, G. L. 1982 Experimental and asymptotic study of nonspherical bubble collapse. *Appl. Sci. Res.* **38**, 187–197.

COLE, R. H. 1948 *Underwater Explosion.* Princeton University Press.

CRUM, L. A. 1975 Bjerknes forces on bubbles in a stationary sound field. *J. Acoust. Soc. Am.* **57**, 1363–1370.

DEAR, J. P. & FIELD, J. E. 1988a A study of the collapse of arrays of cavities. *J. Fluid Mech.* **190**, 409–425.

DEAR, J. P. & FIELD, J. E. 1988b High-speed photography of surface geometry effects in liquid/solid impact. *J. Appl. Phys.* **63**, 1015–1021.

HANSSON, I. & MØRCH, K. A. 1980 The dynamics of cavity clusters in ultrasonic (vibratory) cavitation erosion. *J. Appl. Phys.* **51**, 4651–4658.

KLING, C. L. & HAMMITT, F. G. 1972 A photographic study of spark-induced cavitation bubble collapse. *Trans. ASME* D: *J. Basic Engng* **94**, 825–833.

KNAPP, R. P., DAILY, J. W. & HAMMITT, F. G. 1970 *Cavitation.* McGraw-Hill.

LAUTERBORN, W. 1974 Kavitation durch Laserlicht. *Acustica* **31**, 51–78.

LAUTERBORN, W. & BOLLE, H. 1975 Experimental investigation of cavitation-bubble collapse in neighbourhood of a solid boundary. *J. Fluid Mech.* **72**, 391–399.

LAUTERBORN, W. & HENTSCHEL, W. 1985 Cavitation bubble dynamics studied by high speed photography and holography: Part 1. *Ultrasonics*, November, 260–268.

LINDAU, O. & LAUTERBORN, W. 2001 Investigation of the counterjet developed in a cavitation bubble that collapses near a rigid boundary. *Proc. Fourth Intl Symp. on Cavitation, Pasadena*, A5.001.

MILNE-THOMSON, L. M. 1968 *Theoretical Hydrodynamics*, 5th Edn. Macmillan.

NAUDÉ, C. F. & ELLIS, A. T. 1961 On the mechanism of cavitation damage by nonhemispherical cavities collapsing in contact with a solid boundary. *Trans. ASME* D: *J. Basic Engng* **83**, 648–656.

OHL, C. D., PHILIPP, A. & LAUTERBORN, W. 1995 Cavitation bubble collapse studied at 20 million frames per second. *Ann. Physik* **4**, 26–34.

PELEKASIS, N. A. & TSAMOPOULOS, J. A. 1993 Bjerknes forces between two bubbles. Part 1. Response to a step change in pressure. *J. Fluid Mech.* **254**, 467–499.

PEREGRINE, D. H., SHOKER, G. & SYMON, A. 1990 The bifurcation of liquid bridges. *J. Fluid Mech.* **212**, 25–30.

PHILIPP, A., DELIUS, M., SCHEFFCZYK, C., VOGEL, A. & LAUTERBORN, W. 1993 Interaction of lithotripter-generated shock waves with air bubbles. *J. Acoust. Soc. Am.* **93**, 2496–2509.

PHILIPP, A. & LAUTERBORN, W. 1998 Cavitation erosion by single laser-produced bubbles. *J. Fluid Mech.* **361**, 75–116.

PLESSET, M. S. & CHAPMAN, R. B. 1971 Collapse of an initially spherical vapour cavity in the neighbourhood of a solid boundary. *J. Fluid Mech.* **47**, 283–290.

RAYLEIGH, LORD 1917 On the pressure developed in a liquid during the collapse of a spherical cavity. *Phil. Mag.* **34**, 94–98.

SATO, K., TOMITA, Y. & SHIMA, A. 1993 Numerical analysis of a gas bubble near a rigid boundary in an oscillatory pressure field. *J. Acoust. Soc. Am.* **95**, 2416–2424.

SHUTLER, N. D. & MESLER, R. B. 1965 A photographic study of the dynamic and damage capabilities of bubbles collapsing near solid boundaries. *Trans. ASME* D: *J. Basic Engng* **87**, 511–517.

TAKAHIRA, H., FUJIKAWA, S. & AKAMATSU, T. 1989 Collapse motion of a single gas bubble near a plane or curved rigid wall. *Trans. Japan Soc. Mech. Engng* **55**, 2720–2728 (in Japanese).

TESTUD-GIOVANNESHI, P., ALLONCLE, A. P. & DUFRESNE, D. 1990 Collective effects of cavitation: Experimental study of bubble–bubble and bubble–shock wave interactions. *J. Appl. Phys.* **67**, 3560–3564.

TOMITA, Y., BLAKE, J. R. & ROBINSON, P. B. 1998 Interaction of a cavitation bubble with a curved rigid boundary. *Proc. Third Intl Symp. on Cavitation, Grenoble* (ed. J. M. Michel & H. Kato), pp. 51–56.

TOMITA, Y. & KODAMA, T. 2001 Some aspects of the motion of two laser-produced cavitation bubbles near a free surface. *IUTUM Symp. on Free Surface Flows* (ed. A. C. King & Y. D. Shikhmurzaev), pp. 303–310. Kluwer.

TOMITA, Y., KODAMA, T. & SHIMA, A. 1991 Secondary cavitation due to interaction of a collapsing bubble with a rising free surface. *Appl. Phys. Lett.* **59**, 274–276.

TOMITA, Y., OBARA, T., TAKAYAMA, K. & KUWAHARA, M. 1994 Cavitation phenomena in extracorporeal microexplosion lithotripsy. *Shock Waves* **3**, 149–157.

TOMITA, Y., SATO, K. & SHIMA, A. 1992 Theoretical and experimental investigations on the nonspherical motion of a bubble near a plane rigid wall. *Trans. Japan Soc. Mech. Engng* **59**, 1891–1899 (in Japanese).

TOMITA, Y., SATO, K. & SHIMA, A. 1994 Interaction of two laser-produced cavitation bubbles near boundaries. In *Bubble Dynamics and Interface Phenomena* (ed. J. R. Blake, J. M. Boulton-Stone & N. H. Thomas), pp. 33–45. Kluwer.

TOMITA, Y. & SHIMA, A. 1986 Mechanisms of impulsive pressure generation and damage pit formation by bubble collapse. *J. Fluid Mech.* **169**, 535–564.

TOMITA, Y. & SHIMA, A. 1990 High-speed photographic observations of laser-induced cavitation bubbles in water. *Acustica* **71**, 161–171.

TOMITA, Y., SHIMA, A. & TAKAHASHI, H. 1991 The behavior of a laser-produced bubble near a rigid wall with various configurations. *Proc. Cavitation '91 Symp., The First Joint ASME–JSME Fluids Engng Conf., Portland* (ed. O. Furuya & H. Kato), pp. 19–25.

TOMITA, Y., SHIMA, A. & TAKAYAMA, K. 1989 Formation and limitation of damage pits caused by bubble-shock wave interaction. *Proc. 1988 National Symp. on Shock Wave Phenomena* (ed. K. Takayama), pp. 149–160. Institute of Fluid Science, Tohoku University, Sendai.

TOMITA, Y., TSUBOTA, M., NAGANE, K. & AN-NAKA, N. 2000 Behavior of laser-induced cavitation bubbles in liquid nitrogen. *J. Appl. Phys.* **88**, 5993–6001.

TONG, R. P., SCHIFFERS, W. P., SHAW, S. J., BLAKE, J. R. & EMMONY, D. C. 1999 The role of 'splashing' in the collapse of a laser-generated cavity near a rigid boundary. *J. Fluid Mech.* **380**, 339–361.

TULIN, M. P. 1969 On the creation of ultra-jets. In *L. I. Sedov 60th Anniversary Volume: Problems of Hydrodynamics and Continuum Mechanics*, pp. 725–747. SIAM.

VAN DER MEULEN, J. H. J. 1994 On laser-induced cavitation bubbles and the impact on nearby solid boundaries. *Proc. Second Intl Symp. on Cavitation, Tokyo* (ed. H. Kato), pp. 249–256.

VOGEL, A., LAUTERBORN, W. & TIMM, R. 1989 Optical and acoustic investigations of the dynamics of laser-produced cavitation bubbles near a solid boundary. *J. Fluid Mech.* **206**, 299–338.

ZHANG, S., DUNCAN, J. H. & CHAHINE, G. L. 1993 The final stage of the collapse of a cavitation bubble near a rigid wall. *J. Fluid Mech.* **257**, 147–187.

ZHONG, P., COCKS, F. H., CIOANTA, I. & PREMINGER, G. M. 1997 Controlled, forced collapse of cavitation bubbles for improved stone fragmentation during shock wave lithotripsy. *J. Urology* **158**, 2323–2328.